ACS Catalysis

Research Article

pubs.acs.org/acscatalysis

Mechanistic Study of Codoped Titania with Nonmetal and Metal Ions: A Case of C + Mo Codoped TiO_2

Yan-Fang Li,[†] Danhua Xu,[‡] Jeong Il Oh,[‡,⊥] Wenzhong Shen,[‡] Xi Li,*[,§] and Ying Yu*[,†]

[†]Institute of Nanoscience and Nanotechnology, Central China Normal University, Wuhan 430079, China

[‡]Department of Physics, Shanghai Jiao Tong University, Shanghai 200240, China

[§]Department of Environmental Science and Engineering, Fudan University, Shanghai 200433, China

[⊥]Department of Physics, Boston College, Chestnut Hill, Massachusetts 02467, United States

Supporting Information

ABSTRACT: To study the mechanism of metal- and nonmetal-ion-doped TiO_2, TiO_2 codoped with carbon and molybdenum prepared by a hydrothermal method following calcination post-treatment is chosen as the study object. The prepared samples are characterized by X-ray diffractometer, Raman spectroscopy, X-ray photoelectron spectroscopy, and Brunauer–Emmett–Teller measurement. It is found that the doped carbon exists in the form of deposited carbonaceous species on the surface of TiO_2, and molybdenum substitutes for titanium in the lattice and exists as the Mo^{6+} state. All the prepared samples have comparable large surface areas. The photocatalytic activities are tested by degradation of rhodamine-B and acetone under visible light irradiation. The results show that the codoped sample has the best performance in the degradation of both RhB and acetone. Briefly, the enhanced photocatalytic activity of codoped TiO_2 is the synergistic effect of C and Mo. Mo substitutes in the Ti site in the lattice for the formation of the doping energy level, and C exists as carbonaceous species on the surface of the TiO_2, which can absorb visible light. The synergetic effects of C and Mo not only enhance the adsorption of visible light but also promote the separation of photogenerated electrons and holes, which consequently contribute to the best photodegradation efficiency of organic pollutants under visible-light irradiation. UV–vis diffuse reflectance spectra and photoluminescence spectra of the prepared samples and fluorescence of terephthalic acid for the detection of hydroxide radical are employed to verify the proposed mechanism.

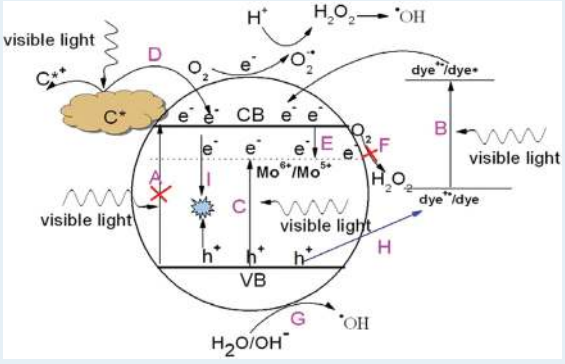

KEYWORDS: *TiO_2, metal and nonmetal codoping, mechanism, C and Mo*

1. INTRODUCTION

Recently, the environmental problem has become increasingly serious, and water pollution caused by an increase in the world population and the expansion of chemical and textile industries are two of the most serious issues to be solved. Heterogeneous semiconductor photocatalysis is considered to be an effective method for wastewater treatment, and many related studies have been performed.[1−3] Titania or titanium dioxide (TiO_2) is one of the most promising semiconductor photocatalysts owing to its long-term stability, nontoxicity, and excellent photocatalytic property; however, there are two aspects limiting its application. On one hand, the wide band gap nature of titania (3.2 eV for the anatase structure or 3.0 eV for the rutile structure) makes it absorb only ultraviolet (UV) light, which limits the effective usage of solar light. On the other hand, the recombination rate of photogenerated electron–hole pairs is too high to be used for organic pollutant degradation in practice.[4]

Doping is a promising approach to extend the spectral response of TiO_2 to the visible region.[5−13] Moreover, this approach can also effectively enhance the interfacial charge transfer and lower the electron–hole recombination rate.[14,15] More recently, codoping of both metal and nonmetal elements into TiO_2 have attracted considerable interest since codoped TiO_2 presents better photocatalytic activity and some particular characteristics. The advantages of codoping have been demonstrated in several systems, such as N/Fe,[16] V/N,[17] N/Sn,[18] C/V,[19] etc.

To illustrate their enhanced photocatalytic performance, several kinds of mechanisms are proposed. There are two representative views. One is that both the doping elements including metal and nonmetal are doped into the lattice of TiO_2 for the formation of doping energy levels in the band gap of TiO_2, which enhances visible light absorption and thus leads to higher photocatalytic activity.[16,17] The other one is that metal elements prefer to substitute at the Ti site in the lattice for the formation of the doping energy level, and nonmetal

Received: July 10, 2011

   dx.doi.org/10.1021/cs2006668 | ACS Catal. 2012, 2, 391−398

elements exist as surface species that can absorb visible light. The enhanced photocatalytic performance is the result of a synergistic effect of metal and nonmetal ion codoping.[18,19] However, some problems are still present in the proposed mechanisms. First, although the mechanism is proposed in published papers, some processes involved in the transfer of photogenerated carriers are not well demonstrated. Second, there is no direct evidence provided to prove the presence of the proposed intermediates, so it is necessary to illustrate a systematic and comprehensive mechanism and conduct corresponding experiments to support it.

Among all nonmetal doping, carbon-doped TiO_2 exhibits superior photocatalytic activity under visible light.[6,20,21] Mo doping as metal ion doping is also considered an effective approach to improve the photocatalytic activity of TiO_2.[22,23] To the best of our knowledge, few studies have focused on carbon- and molybdenum-codoped TiO_2. Pan et al.[24] prepared C + Mo-codoped TiO_2 powers by a thermal oxidation method, and the codoped TiO_2 had an enhanced photocatalytic activity under UV light. Another published work about carbon- and molybdenum-codoped TiO_2 was carried out by Liu et al. They revealed that the codoped sample exhibited better activity under visible light.[25] Nevertheless, the mechanism of such an enhanced photocatalytic activity in TiO_2 through the C + Mo codoping has not been discussed convincingly.

In this study, C + Mo-codoped titania was prepared by hydrothermal treatment of P-25 with NaOH aqueous solution and Mo and C doping sources. Then the prepared samples were characterized and their photocatalytic activity was tested through the degradation of rodamine-B (RhB) and acetone. In addition, a comprehensive mechanism for C + Mo-codoped titania is illustrated, and extra experiments are also conducted to provide evidence for the mechanism.

2. EXPERIMENTAL SECTION

2.1. Sample Preparation. C + Mo-codoped titania samples were fabricated by using a hydrothermal calcining process, similar to that in ref 26. We employed commercial TiO_2 powder (Degussa P25) and sodium hydroxide as raw materials, and ammonium heptamolybdate tetrahydrate ($(NH_4)_6Mo_7O_{24}\cdot 4H_2O$) and glucose as the Mo and C doping sources, respectively. Note that all the chemicals used were of analytic grade so that they did not need further purification.

For the sample fabrication procedure, Degussa P25 (0.75 g) was mixed with a 10 M NaOH solution (70 mL), then $(NH_4)_6Mo_7O_{24}\cdot 4H_2O$ and glucose, containing 2 at. % of Mo and 1 at. % of C, respectively, were added to the mixed solution. This mixture was then stirred for 0.5 h for dispersion, and the dispersed mixture was transferred into a Teflon-lined stainless steel autoclave (100 mL volume) for hydrothermal treatment at 150 °C. After 48 h of hydrothermal treatment, the precipitate (white) was separated from the supernatant by centrifugation and washed with double distilled water and 0.1 M HCl solution several times until the pH value reached around 6.5. The washed sample was then dried in a vacuum oven at 80 °C for 12 h and, finally, calcined at 400 °C for 1 h. Note that we used the same hydrothermal calcining technique as described above to synthesize single material (Mo and C)-doped and undoped TiO_2.

2.2. Characterization. X-ray diffraction (XRD) measurements were carried out using a Y-2000 diffractometer (D/max 30 kv) with Cu Kα radiation (λ = 0.154 178 nm) at a scan rate of 0.06° $2\theta\cdot s^{-1}$ for the characterization of the crystalline phase, phase composition, and crystallite size. To probe structural change at a micrometer scale, Raman spectra were recorded at room temperature using a Jobin Yvon LabRAM HR 800UV micro-Raman system under Ar^+ (514.5 nm) laser excitation. UV−vis diffuse reflectance spectra were obtained with a PerkinElmer Lambda35 spectrophotometer. For analyzing surface chemicals, X-ray photoelectron spectroscopy (XPS) was performed in a PHI Quantum 2000 XPS system with a monochromatic Al Kα source and charge neutralizer. Nitrogen adsorption/desorption isotherms and the Brunauer−Emmett−Teller (BET) specific surface area (S_{BET}) were obtained from a Micromeritics ASAP 2010 analyzer (accelerated surface area and porosimetry system), in which all the samples were degassed at 100 °C prior to BET measurements. The Barret−Joyner−Halender (BJH) method was used to determine the pore size. The photoluminescence (PL) spectra of the prepared samples were measured by a photoluminescence spectrometer (PerkinElmer Lambda 55). The formation of hydroxyl radicals (·OH) on the surface of the prepared samples in water under visible light was detected by a terephthalic acid (TA) probe method.[27] The PL spectra of generated 2-hydroxyterephthalic acid (TAOH) were measured by using the same fluorescence spectrophotometer as the above.

2.3. Photocatalytic Activity Measurements. The photocatalytic activity of the prepared samples was examined via the photocatalytic degradation of rhodamine-B (RhB) and acetone under visible light irradiation. For the degradation of RhB, a 350 W xenon lamp (Lap Pu, XQ) was used as the light source with a 420 nm cutoff filter right above the reactor to remove the irradiation below 420 nm. The experiments were performed in self-constructed beaker-like glassware with double walls for cooling water circulation. The samples (0.1 g) were dispersed in 10 μM RhB aqueous solution (100 mL). Prior to the irradiation, the solution was stirred in the dark for 0.5 h to reach adsorption/desorption equilibrium, then the solution was exposed to light while being continuously stirred. In addition, oxygen aeration was kept in operation with an air pump to ensure a constant supply of oxygen. At intervals of 30 min, 2 mL sample aliquots were removed and centrifuged to remove particles. The collected supernatant was then investigated using a Shimadzu UV-1700 UV−vis spectrophotometer, yielding the residual concentration of RhB.

For the degradation of acetone under visible light irradiation, the experiments were carried on a closed, cylindrical, stainless gas-phase batch reactor with a volume of 7.2 L. A 125 W UV lamp was set on the inner wall of the reactor, and the visible light irradiation (>420 nm) was achieved with a glass filter. The reactor was connected to a GC9560 gas chromatograph (GC) equipped with a flame ionization detector (FID), a methane converter, a Porapak R column, and a PEG20 M column through an automatically sampling 10-way valve (VALCO) with an air actuator. A 0.4 g portion of each catalyst was dispersed onto the surface of three dishes with a diameter of 14 cm. After the dishes with catalyst were placed in the reactor, the lamp was not turned on until the concentration of CO_2 remained stable to ensure all adventitious organic compounds adsorbed on the catalyst are removed. Then a certain amount of acetone was injected with a syringe into the reactor. The concentration of CO_2 produced was obtained by subtracting the initial concentration of CO_2 after the acetone was degraded for 5 min.

dx.doi.org/10.1021/cs2006668 | ACS Catal. 2012, 2, 391−398

3. RESULTS AND DISCUSSION

3.1. Structure and Photocatalytic Property. The XRD patterns in Figure 1 show that all the calcinated samples are of

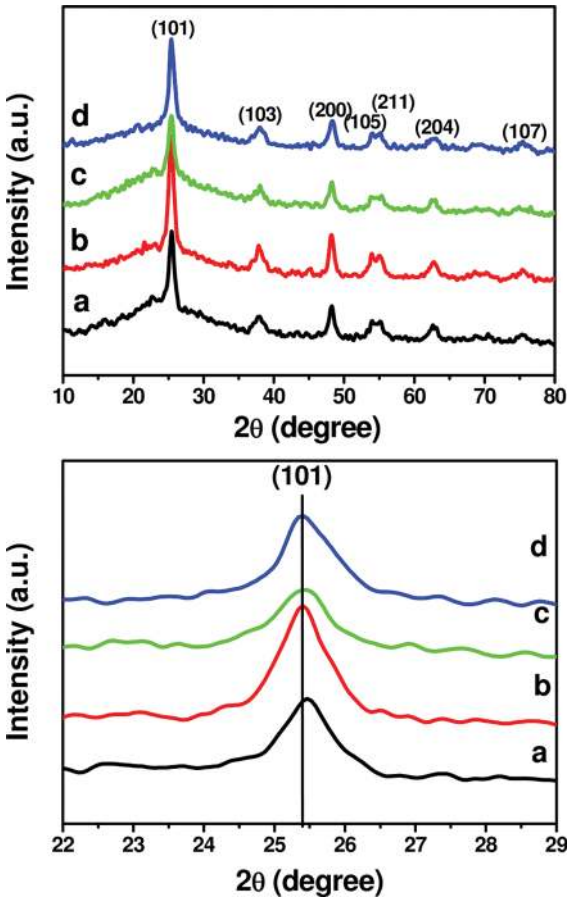

Figure 1. XRD patterns for the calcined samples: (a) C + Mo-codoped, (b) C-doped, (C) Mo-doped, and (d) undoped TiO_2. (lower panel) XRD peaks correspond to the (101) crystal plane of the different TiO_2 samples.

anatase structure, since all of the indexed peaks correspond to the anatase phase of TiO_2 (JCPDS no. 21-1272). Note that there are no visible peaks corresponding to Mo or C. The crystallite sizes of the samples are readily obtained from the Scherrer equation by using the full width at half-maximum of the (101) peak of the anatase phase, as listed in Table 1. The crystalline sizes of pure TiO_2 and C-doped TiO_2 are17.9 and 17.89 nm, respectively, suggesting that a small amount of C doping has no obvious effect on the crystalline size of the TiO_2; however, the crystalline size of the Mo-doped and codoped samples are smaller than that of the undoped one, which indicates that the doping of Mo in TiO_2 can remarkably suppress the growth of TiO_2 nanoparticles. On the basis of the Bragg's law, $2d_{hkl} \sin \Theta = n\lambda$, and the formula for a tetragonal unit cell, $1/(d_{hkl})^2 = (h^2 + k^2)/a^2 + l^2/c^2$, the lattice parameters are calculated and listed in Table 1. The lattice parameters along the *c*-axis decrease as the Mo is doped, indicating that the lattice distortions are caused by the partial substitution of Ti sites by Mo ions.[19] It is known that the ionic radius of Mo^{6+} (0.059 nm) is smaller than that of Ti^{4+} (0.0605 nm). When Ti is replaced by Mo, the lattice will become compacted, which limits the growth of crystallites. Similar phenomena have been observed in many transitional metal doping systems.[13,27]

From the (101) XRD peaks as highlighted in the lower panel of Figure 1, one can see that the peaks slightly shift to higher angles with the doping of C and Mo, and the crystallite size of codoped TiO_2 is between that of the C-doped and Mo-doped samples. These results indicate that carbon and molybdenum have a synergistic effect on each other. Compared with undoped TiO_2, the crystallite size and the position of diffraction peaks of C-doped TiO_2 show no big differences, implying that the influence of carbon doping on the crystal structure is slight.

Raman spectroscopy as a sensitive technique has been employed to examine phase composition and surface homogeneity. As clearly seen in Figure 2, there are five

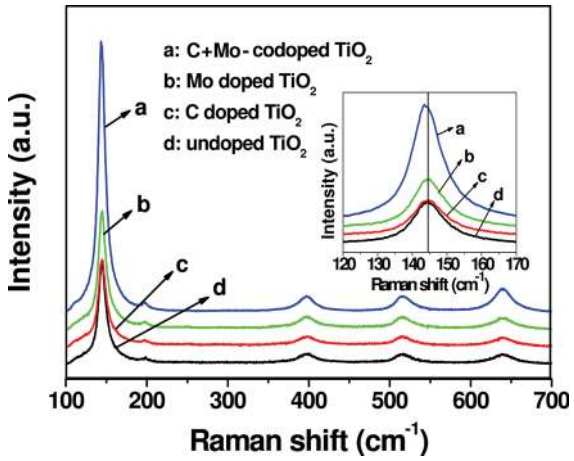

Figure 2. Raman spectra for the calcined samples. The inset shows Raman spectra around the strongest peaks.

Raman peaks at 144, 196, 400, 517, and 640 cm^{-1} for all the calcined samples, corresponding to the E_g, E_g, B_{1g}, A_{1g}, and E_g modes of the anatase phase of TiO_2, respectively.[28] It indicates that the anatase phase dominates the crystalline structure of the calcinated samples, which is consistent with the XRD results. There is no observed Raman peak corresponding to either Mo or C, indicating that all the samples prepared have a

Table 1. Physical Characteristics of Calcined Samples and P25

sample	crystallite size (nm)[a]	lattice parameter (Å)		S_{BET} (m^2 g^{-1})[b]	av pore size (nm)[b]	total pore vol (cm^3/g)[b]
		a	*c*			
undoped TiO_2	17.90	3.7712	9.5174	237.02	23.12	1.3700
Mo-doped TiO_2	8.95	3.7592	9.2408	188.63	26.63	1.2578
C-doped TiO_2	17.89	3.7568	9.6091	183.61	27.32	1.2542
C + Mo-codoped TiO_2	14.92	3.7620	9.3425	176.30	28.41	1.2521
P25				43.3	36.494	0.3954

[a]Determined by XRD using Scherrer equation. [b]Calculated from S_{BET}.

dx.doi.org/10.1021/cs2006668 | ACS Catal. 2012, 2, 391–398

homogeneous structure. Moreover, as can be seen from the inset of the figure, the Raman peak of the codoped TiO_2 at ~144 cm^{-1} (the main E_g anatase vibration mode) exhibits a slight shift to a low wavenumber. As for the monodoped samples, no apparent shift is observed, which is also in accordance with the XRD results.

We used the XPS technique to investigate the surface chemistry of the calcined samples. As in Figure 3, the XPS survey spectra for undoped, C-doped, Mo-doped, and C + Mo-codoped TiO_2 demonstrate that all the samples contain Ti, O, and C elements. Note that the carbon peaks are attributed to adventitious hydrocarbon from the XPS instrument itself or aromatic carbon on the surface of the catalysts.

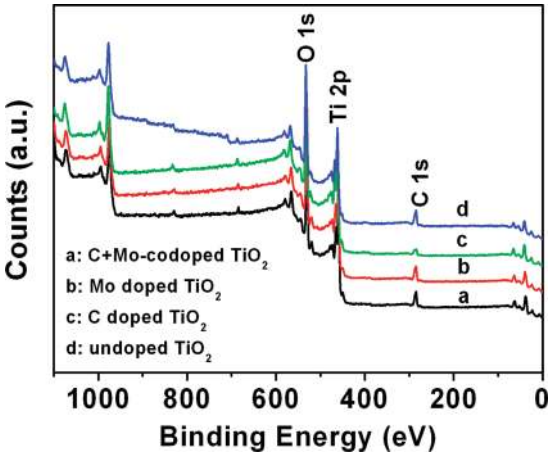

Figure 3. XPS survey spectra for the calcined samples.

In Figures 4a–c, high resolution XPS spectra are presented near the C 1s band for undoped, C-doped, and C + Mo-codoped TiO_2, respectively. Note that the XPS spectrum for Mo-doped TiO_2 is not presented, since it is almost the same as that for undoped TiO_2 near the C 1s band. For all three samples, the main peaks are observed at ~284.7 eV, attributed to adventitious hydrocarbon from the XPS instrument itself or aromatic carbon on the surface of the catalysts. In addition, small peaks are also observed in the cases of C-doped and C + Mo-codoped samples, indicating the presence of C═O bonds in the doped samples. It may be a result of the deposited carbonaceous species on the surface of TiO_2.[19,29] No peak with a binding energy around 282 eV from the C–Ti bond is observed, so the carbon here does not substitute for oxygen in the titania lattice. In addition, compared with pure TiO_2, there is no shift of the Ti 2p binding energies for all the samples (Figure S1 in the Supporting Information); thus, the possibility that carbon elements may be embedded in the lattice without interacting with Ti is excluded. Hereby, the doped carbon very likely exists in the form of deposited carbonaceous species on the surface of TiO_2.

To examine the Mo doping state, the Mo 3d binding state is measured as shown in Figure S2 (in the Supporting Information). The peak at 231.9 eV is attributed to the Mo^{6+} $3d_{5/2}$,[30] which indicates that Mo substitutes titanium in the lattice and exists as Mo^{6+}. Above all, from the XRD and XPS results, we can see that the doped carbon exists in the form of deposited carbonaceous species on the surface of the TiO_2, and Mo replaces titanium in the lattice and presents as Mo^{6+}.

The nitrogen adsorption/desorption isotherms of the calcined samples are shown in Figure 5a. As shown in the figure, all the samples have the isotherms of type IV with distinct hysteresis loops observed in the range of 0.75–1.0 P/P_0. These are called the H3 hysteresis loop that is the characteristic of mesoporous materials (2–50 nm).[31] Figure 5b shows that all the samples have wide pore-size distributions from 1 to 40 nm with a maximum pore diameter of about 8 nm. In addition, the S_{BET} and pore volumes derived from the nitrogen adsorption/desorption isotherms for calcined samples are listed in Table 1. It can be seen that the surface area and pore size significantly increase compared with those for the precursor of P25: for example, 43.3 m^2/g and 0.3954 cm^3/g (P25) → 176.30 m^2/g and 1.2521 cm^3/g (codoped sample),

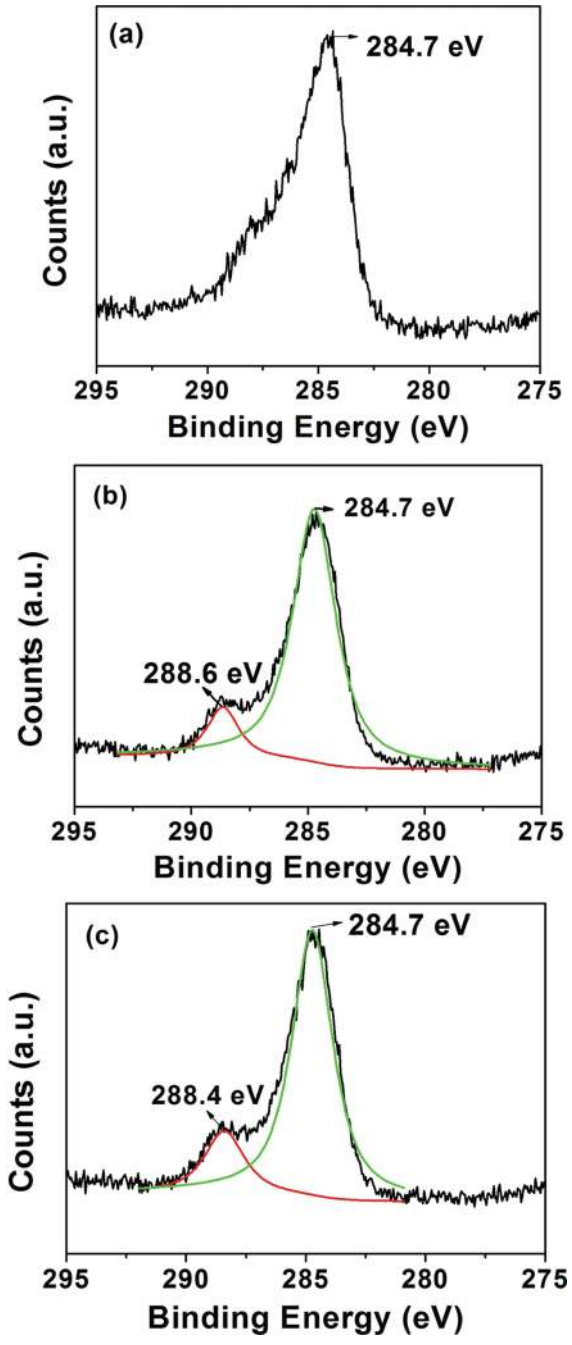

Figure 4. High-resolution XPS spectra for calcined samples around C 1s: (a) undoped, (b) C-doped, and (c) C + Mo-codoped TiO_2. The green and red curves in b and c are Gaussian fittings in the presence of adventitious carbons and C═O bonds, respectively.

dx.doi.org/10.1021/cs2006668 | ACS Catal. 2012, 2, 391–398

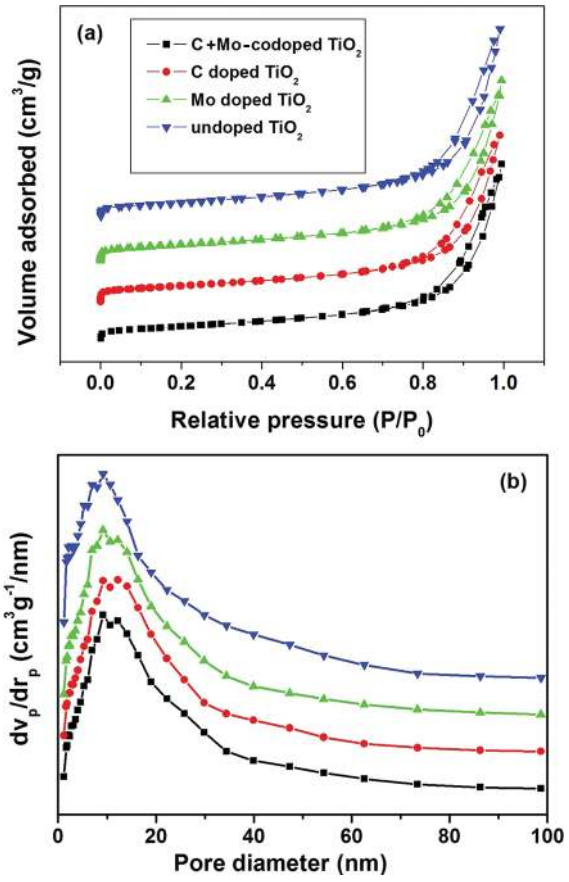

Figure 5. (a) N_2 adsorption/desorption isotherm plot. (b) BJH pore size distribution plot. Note that all other curves except for C + Mo-codoped TiO_2 (black squares) are shifted upward for clarity. In the measurement of the N_2 adsorption/desorption isotherm, P_0 in relative pressure P/P_0 is set to 104.7 Kpa.

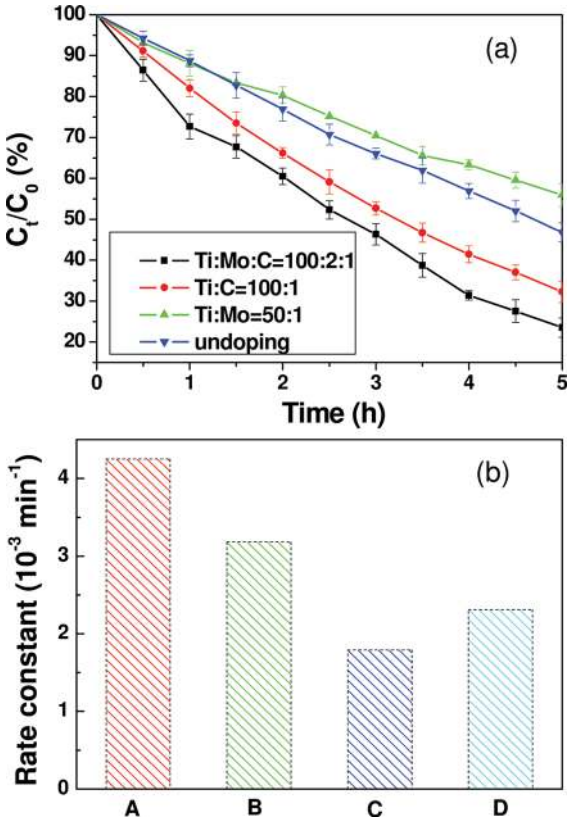

Figure 6. (a) Time-dependent photodegradation efficiency of RhB and (b) apparent reaction rate constants of the prepared samples of C + Mo-codoped TiO_2 (A), C-doped TiO_2 (B), Mo-doped TiO_2 (C), and undoped TiO_2 (D).

respectively. These increased S_{BET} and pore volumes may imply an enhanced capability for organic pollutant adsorption, leading to the improvement of photocatalytic activity for the calcined samples. Moreover, the N_2 adsorption/desorption isotherms and the pore size distributions of C and Mo doped samples are not much different from that of the undoped sample, implying that all the samples have a comparable surface area and a similar number of reaction sites on their surface.

3.2. Photocatalytic Activity of Catalyst. The photocatalytic activity of the calcinated samples was first evaluated by the photodegradation of RhB. RhB was stable under visible light irradiation in the absence of any catalyst. Figure 6a shows the photodegradation efficiency of RhB over different samples as a function of time under visible light irradiation. Temporal changes in the concentration of RhB were monitored by examining the absorption in UV−vis spectra at 553.5 nm. Before turning on the xenon lamp, almost no intensive adsorption of RhB on the surface of the prepared catalysts was observed in the dark, so the disappearance of RhB originates mainly from photocatalytic degradation. As can be seen in Figure 6, both C-doped and C + Mo-codoped samples show much better photocatalytic activity than the undoped sample, and the codoped sample displays the best performance; however, the Mo-doped sample exhibits poorer photocatalytic activity than the undoped sample. The probable mechanism will be discussed later. The photodegradation efficiencies of RhB over different samples are also characterized by the apparent reaction rate constant, k, which can be calculated using the equation: $\ln(C_0/C) = kt$, with C_0 and C being the initial concentration and the reaction concentration of RhB, respectively. The results are shown in Figure 6b. C + Mo-codoped TiO_2 has the highest apparent reaction rate constant, $\sim 4.25 \times 10^{-3}$ min^{-1}, which is ~2 times that of the undoped one.

The spectral changes in the RhB solutions under visible light irradiation are displayed in Figure S3 (in the Supporting Information). It can be seen from the figure that as time increases, the absorption peak shows a blue shift with the decrease in the peak intensity. Note that RhB degradation occurs via two competitive processes: de-ethylation or cleavage of RhB chromophore ring structure.[32] Generally speaking, the weakening of the absorption band comes from the cleavage of the RhB chromophore ring structure, and the gradual hypochromic shift of the absorption maximum is caused by the N-deethylation of RhB molecules.[33−35] Among all the samples, both the intensity of the peak around 553.5 nm and the absorption maximum change the most for C + Mo-codoped titania.

The time-dependent wavelength shift for the absorption maximum is shown in Figure 7, which confirms the de-ethylation process for RhB degradation. In addition, the color of the suspension faded gradually during photocatalytic experiment, indicating the RhB chromophore ring structure is destroyed simultaneously.[36] Therefore, in the degradation of RhB with all of the prepared samples as photocatalysts, the mechanism may follow both the de-ethylation process and the process of the chromospheres ring structure cleavage in RhB. It

dx.doi.org/10.1021/cs2006668 | ACS Catal. 2012, 2, 391−398

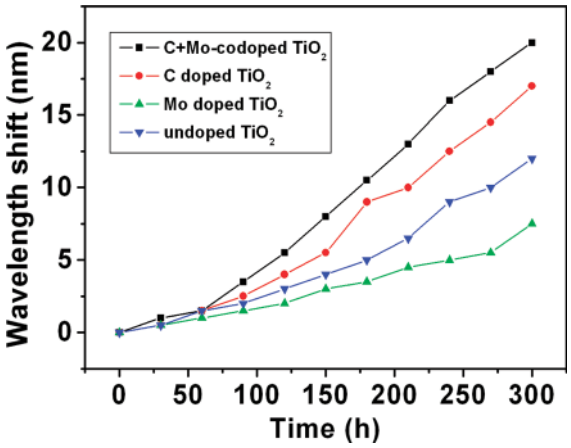

Figure 7. Time-dependent wavelength shift of the major absorption peak of RhB under visible light irradiation.

was reported that de-ethylation of the fully *N,N,N,N*-tetraethylated rhodamine molecule of λ_{max} = 552 nm (i.e., RhB) has the wavelength position of its major absorption band moving toward the blue region, such as *N,N,N*-triethylated rhodamine, 539 nm; *N,N*-diethylated rhodamine, 522 nm; *N*-ethylated rhodamine, 510 nm; and rhodamine, 498 nm.[33,34] In this study, the C + Mo-codoped titania has the largest λ_{max} shift, from 553.5 to 531 nm, which means that just one ethyl group is destroyed. Therefore, it is much more possible for the degradation mechanism to mainly follow the degradation route of the cleavage of the RhB chromophore ring structure in this system.

The photocatalytic activity for the prepared samples for acetone degradation (gas-phase photocatalysis) under visible light irradiation was also tested. The results are shown in Figure S4 (in the Supporting Information). From the figure, we can see that the C + Mo-codoped TiO_2 and C-doped TiO_2 exhibit a higher ability for CO_2 production from acetone degradation than undoped TiO_2. In addition, Mo-doped titania also shows better activity than pure TiO_2 in the process of acetone degradation, which is different from RhB degradation. From the above results of both RhB and acetone degradation, we can come to the conclusion that C + Mo-codoped TiO_2 indeed does have a better photocatalytic activity than the updoped one.

3.3. Mechanism Discussion. On the basis of the observed photocatalytic activities and the characterizations shown above, a probable mechanism about the photodegradation of RhB is illustrated in Scheme 1. Since all of the samples have a comparable surface area and pore volume and the number of reaction sites on the samples may be similar, the difference in the photocatalytic activity can be related to the structure. Different structures lead to different sources of photogenerated carriers and their transfer route. TiO_2 is a wide band gap semiconductor, so its band gap cannot be excited upon visible light, implying that process A (i.e., one route to photogenerating electron−hole pairs) cannot occur. It is known that RhB can be excited by visible light and injects electrons into the conduction band of TiO_2 (process B), so the injected electrons react with O_2 molecules that are adsorbed on the TiO_2 surface to yield the $O_2^{\bullet-}$ radical anion and, subsequently, the HO· radical by protonation.[32] Therefore, in this case, RhB can be degraded in even an undoped TiO_2 system, although its photodegradation efficiency is not high.

Scheme 1. Schematic Diagram of Generation and Transfer of Electrons and Holes for C + Mo-Codoped TiO_2 in the Degradation of RhB under Visible Light Irradiation[a]

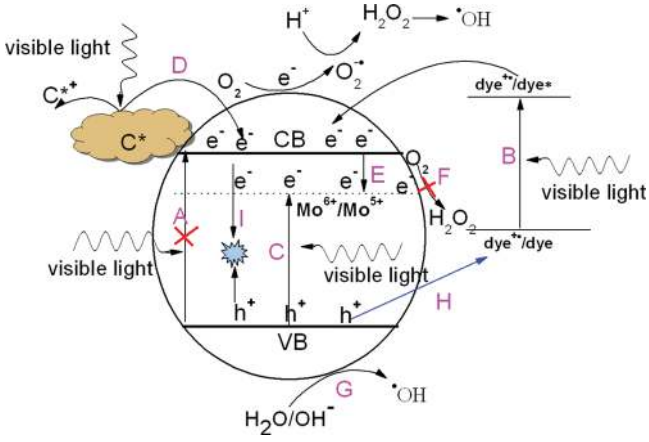

[a]There are nine processes as follows: (A, C) the processes of photogeneration of electron-hole pairs, (B) the process of dye sensitization under visible light, (D) the sensitization process of carbonaceous carbons on the surface of TiO_2, (E) the process of electron capture from the conduction band of TiO_2, (F) the process of hydrogen peroxide formation by the interaction between photoexcited electrons and oxygen, (G) the process of hydroxide radical formation by the interaction between photogenerated holes and H_2O/OH^-, (H) the process of dye oxidation by photogenerated holes directly, and (I) the process of recombination of electrons and hole.

As discussed in the XRD patterns and XPS spectra, molybdenum substitutes for titanium in the lattice and exists as the state of Mo^{6+}. The doping energy level of Mo^{6+}/Mo^{5+} is 0.4 eV,[12,37] which is much more positive than the potential of the conduction band of TiO_2 particles [E_{cb} = −0.5 eV vs NHE (normal hydrogen electrode) at pH = 1].[38] Therefore, after doping with Mo, the electrons can be excited from the valence band to the Mo^{6+}/Mo^{5+} doping energy level under visible light (process C). In addition, the energy of Mo^{6+}/Mo^{5+} is below the conduction band of TiO_2, so it is easy for Mo^{6+} to capture an injected electron by RhB from the conduction band (process E). The electrode potential of O_2/H_2O_2 is 0.34 eV,[39] which is above the energy level of Mo^{6+}/Mo^{5+}. Therefore, the electrons on the Mo^{6+}/Mo^{5+} level cannot react with O_2 to form H_2O_2/HO·, and process F cannot occur.

Now we want to note that the Mo doped TiO_2 shows a negative effect on the photodegradation of RhB, as shown in Figure 6, which is different from the previous studies.[12,23] Many factors can affect the photocatalytic activity of samples, such as the preparation method, the doping concentration, the dopant energy level within the TiO_2 lattice, and the distribution of the dopant in the particle.[14] In addition, the metal ion dopant can act as a mediator of interfacial charge transfer or as a recombination center, so there is an optimal value for the dopant concentration.[40] Here, the doping energy level of Mo^{6+}/Mo^{5+} has three functions: First, it can capture electrons from the conduction band that injected from the dye (process E), and thus, the number of hydroxide radicals is reduced. Second, electrons can be excited to the Mo^{6+}/Mo^{5+} energy level, and then the holes leaving on the valence band can degrade organic pollutants (process G and H). Third, the Mo^{6+}/Mo^{5+} energy level can be the recombination center if the dopant concentration is not proper (process I). These three processes compete with each other, so it is critical to find an

dx.doi.org/10.1021/cs2006668 | ACS Catal. 2012, 2, 391−398

optimal dopant concentration. In our experiment, from the results of the photocatalytic activity, we can deduce that processes E and I prevail over processes G and H, with a Mo doping concentration of 2 at. %, resulting in the poor photocatalytic performance of Mo-doped TiO_2.

The C element in the doped samples is present in the form of carbonaceous species deposited on the surface that is labeled as C* in Scheme 1. It has been suggested[19,29] that the carbon species coated on the surface has a sensitization effect under visible light. From the UV−vis spectra (Figure S5 in the Supporting Information), we can see that compared with pure TiO_2, C-doped TiO_2 presents an obviously enhanced absorption of visible light, which is direct evidence that the carbon species coated on the surface can greatly promote the photon absorption of TiO_2 in the region of visible light. With the effect of sensitization, the carbon species on the surface can transfer electrons to the conduction band of TiO_2 (process D), which is beneficial to RhB photodegradation, so the C-doped TiO_2 shows better activity than the undoped one.

As for the codoped TiO_2, carbon and molybdenum codoping may have a synergistic effect on each other, as illustrated in the XRD patterns and Raman spectra. This synergistic effect inhibits the recombination of photogenerated holes and electrons on the Mo^{6+}/Mo^{5+} doping energy level, which can be confirmed by the PL spectra shown in Figure 8. PL emission

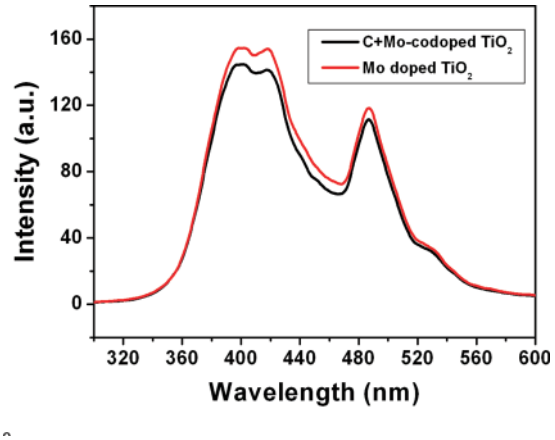

Figure 8. PL spectra of Mo-doped TiO_2 and C + Mo-codoped TiO_2.

results from the recombination of photoinduced charge carriers. The stronger the PL signal, the higher the recombination rate of the photoinduced charge carriers.[16,41] The intensity of C + Mo-codoped TiO_2 is lower than that of mono-Mo-doped TiO_2, indicating that the recombination rate is lower in the codoped sample. When the recombination rate decreases, more photogenerated charge carriers can participate in dye photodegradation, resulting in the enhancement of photocatalytic activity. In addition, in the UV−vis spectra (Figure 5S in the Supporting Information, the C + Mo-codoped sample shows a strong absorption in the visible light region from 420 to 800 nm, and the absorption intensity is much higher than that of C or Mo monodoped TiO_2. It means that with the presence of C and Mo, the codoped titania is more sensitive to visible light, which is also an important factor for the improvement of the photocatalytic performance of TiO_2 under visible light. Therefore, the synergetic effect of C and Mo not only enhances the absorption of visible light, but also promotes the separation of photogenerated electrons and holes, which contribute to the best photodegradation efficiency of organic pollutions under visible light irradiation.

From the mechanism, we can deduce that the hydroxyl radicals are the main reactive species in the photocatalytic oxidation of RhB. In addition, for the Mo-doped and codoped TiO_2, holes are also important reactive species. To further verify the mechanism, the production of major reactive species, hydroxyl radicals, was monitored by a PL technique using TA as the fluorescence probe. TA easily reacts with hydroxyl radicals to generate highly fluorescent hydroxyl terephthalic acid. Thus, the amount of hydroxyl radicals can be quantified by measuring the fluorescence of TAOH.[16] The change in the fluorescence intensity in suspension solution with the prepared samples under visible light irradiation is shown in Figure 9. It

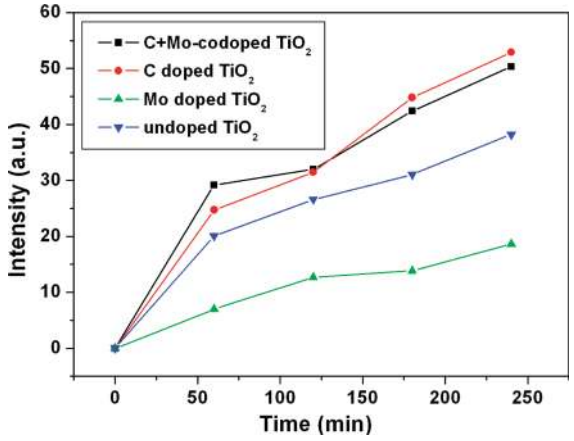

Figure 9. Plots of the induced PL intensity at 425 nm against irradiation time for terephthalic acid on the prepared samples.

can be seen that the amounts of the hydroxyl radicals produced over C-doped and C + Mo-codoped TiO_2 are larger than those over Mo-doped and undoped ones, which is consistent with the photocatalytic activity result shown in Figure 6. With respect to codoped TiO_2, holes also participate in photocatalytic oxidation of RhB. Therefore, although the HO· produced over C-doped TiO_2 is a little higher than that over codoped sample, the C + Mo-codoped TiO_2 still has better photocatalytic activity than the C-doped one.

As for the gas phase photocatalytic oxidation of acetone, the dye sensitization process no longer exists. Thus, the mechanism is a little different. Except for the process of dye sensitization, the explanations for C + Mo codoped TiO_2, C-doped TiO_2, and undoped TiO_2 are still effective here. The difference from RhB degradation is that Mo-doped TiO_2 exhibits higher photocatalytic activity for acetone degradation than pure TiO_2. As discussed above, after doping with Mo, the electrons can be excited from the valence band to the Mo^{6+}/Mo^{5+} doping energy level under visible light, leaving holes in the valence band. Both the holes and electrons can participate in the process of acetone degradation. Therefore, Mo-doped TiO_2 has a better photocatalytic performance than pure TiO_2.

4. CONCLUSIONS

To study the mechanism of TiO_2 codoped with nonmetal and metal, C + Mo-codoped TiO_2 as a model together with undoped, C-doped, and Mo-doped TiO_2, respectively, was successfully synthesized by a simple hydrothermal method following post-treatment. All the samples have a large and

dx.doi.org/10.1021/cs2006668 | ACS Catal. 2012, 2, 391−398

comparable specific surface and porous structure; however, the C + Mo-codoped TiO_2 have the best photocatalytic activity for the degradation of RhB and acetone under visible light irradiation. Mo doping has a negative effect on the degradation of RhB, but a positive effect on the degradation of acetone. The mechanism for the phenomenon is that the enhanced photocatalytic activity of codoped TiO_2 is the synergetic effect of C and Mo. Mo substitutes for the Ti site in the lattice, which forms a doping energy level while C exists as carbonaceous species on the surface of the TiO_2, leading to visible light absorption. The synthetic effects of C and Mo not only improve the absorption of visible light but also promote the separation of photogenerated electrons and holes. Both of them contribute to the best photodegradation efficiencies of organic pollutants over the codoped sample under visible light irradiation. This study can provide theoretical insight into the enhancement of photocatalytic activity of TiO_2 by a nonmetal and metal codoping method.

■ ASSOCIATED CONTENT

Supporting Information

High-resolution XPS spectra of Ti 2p for the prepared samples, high resolution XPS spectrum for Mo 3d for Mo doped TiO_2 (10 at. %), wavelength-dependent temporal UV−vis spectra of the prepared samples in 1.0×10^{-5} M RhB solution for various visible-light irradiation times, time courses of CO_2 produced from acetone oxidation on the prepared samples, and UV−vis spectra of the prepared samples.This material is available free of charge via the Internet at http://pubs.acs.org.

■ AUTHOR INFORMATION

Corresponding Author

*(X.L.) Phone: (+86) 21-65642789. E-mail: xi_li@fudan.edu.cn. (Y.Y.) Phone: (+86) 27-67867037. E-mail: yuying@phy.ccnu.edu.cn.

■ ACKNOWLEDGMENTS

This work was financially supported by the National Natural Science Foundation of China (Nos. 20973070 and 10734020), the National Basic Research Program of China (No. 2009CB939704), the Key Project of the Ministry of Chinese Education (No. 109116), the Key Project of the National Science Foundation of Hubei Province (No. 2011CDA092), and self-determined research funds of CCNU from the college's basic research and operation of MOE. X. Li is indebted to the Fudan-Haoqing foundation at Fudan University of China, and Shanghai Pujiang Rencai Project (No. 09PJ1401400), China.

■ REFERENCES

(1) Tang, J. W.; Zou, Z. G.; Ye, J. H. *Angew. Chem., Int. Ed.* **2004**, *43*, 4463.
(2) Hu, J. S.; Ren, L. L.; Guo, Y. G.; Liang, H. P.; Cao, A. M.; Wan, L. J.; Bai, C. L. *Angew. Chem., Int. Ed.* **2005**, *44*, 1269.
(3) Fu, H. B.; Pan, C. S.; Yao, W. Q.; Zhu, Y. F. *J. Phys. Chem. B* **2005**, *109*, 22432.
(4) Chen, X. B.; Mao, S. S. *Chem. Rev.* **2007**, *107*, 2891.
(5) Asahi, R.; Morikawa, T.; Ohwaki, T.; Aoki, K.; Taga, Y. *Science* **2001**, *293*, 269.
(6) Sakthivel, S.; Kisch, H. *Angew. Chem., Int. Ed.* **2003**, *42*, 4908.
(7) Ohno, T.; Mitsui, T.; Matsumura, M. *Chem. Lett.* **2003**, *32*, 364.
(8) Zhou, J. K.; Lv, L.; Yu, J. Q.; Li, H. L.; Guo, P. Zh.; Sun, H.; Zhao, X. S. *J. Phys. Chem. C* **2008**, *112*, 5316.
(9) Klosek, S.; Raftery, D. *J. Phys. Chem. B* **2001**, *105*, 2815.
(10) Bettinelli, M.; Dallacasa, V.; Falcomer, D.; Fornasiero, P.; Gombac, V.; Montini, T.; Romanò, L.; Speghini, A. *J. Hazard. Mater.* **2007**, *146*, 529.
(11) Araña, J.; Díaz, O. G.; Saracho, M. M.; Rodríguez, J. M. D.; Melián, J. A. H.; Peña, J. P. *Appl. Catal., B* **2001**, *32*, 49.
(12) Yang, Y.; Li, X. J.; Chen, J. T.; Wang, L. Y. *J. Photochem. Photobiol. A* **2004**, *163*, 517.
(13) Zhu, J. F.; Deng, Z. G.; Chen, F.; Zhang, J. L.; Chen, H. J.; Anpo, M.; Huang, J. Z.; Zhang, L .Z. *Appl. Catal., B* **2006**, *62*, 329.
(14) Choi, W.; Termin, A.; Hoffmann, M. R. *J. Phys. Chem.* **1994**, *98*, 13669.
(15) Zhang, H. R.; Tan, K. Q.; Zheng, H. W.; Gu, Y. Z.; Zhang, W. F. *Mater. Chem. Phys.* **2011**, *125*, 156.
(16) Yang, M. J.; Hume, C.; Lee, S.; Son, Y.-H.; Lee, J.-K. *J. Phys. Chem. C* **2010**, *114*, 15292.
(17) Liu, J. W.; Han, R.; Zhao, Y.; Wang, H. T.; Lu, W. J.; Yu, T. F.; Zhang, Y. X. *J. Phys. Chem. C* **2011**, *115*, 4507.
(18) Wang, E. J.; He, T.; Zhao, L. S.; Chen, Y. M.; Cao, Y. A. *J. Mater. Chem.* **2011**, *21*, 144.
(19) Liu, H. B.; Wu, Y. M.; Zhang, J. L. *ACS Appl. Mater. Interfaces* **2011**, *3*, 1757.
(20) Ren, W. J.; Ai, Z. H.; Jia, F. L.; Zhang, L. Z.; Fan, X. X.; Zou, Z. G. *Appl. Catal., B* **2007**, *69*, 138.
(21) Wang, H. Q.; Wu, Z. B.; Liu, Y. *J. Phys. Chem. C* **2009**, *113*, 13317.
(22) Gomathi Devi, L.; Narasimha Murthy, B. *Catal. Lett.* **2008**, *125*, 320.
(23) Štengl, V.; Bakardjieva, S. *J. Phys. Chem. C* **2010**, *114*, 19308.
(24) Zhang, J.; Pan, C. X.; Fang, P. F.; Wei, J. H.; Xiong, R. *ACS Appl. Mater. Interfaces* **2010**, *2*, 1173.
(25) Dong, P. Y.; Liu, B.; Wang, Y. H.; Pei, H. H. *J. Mater. Res.* **2010**, *25*, 2392.
(26) Yu, J. G.; Yu, H. G.; Cheng, B.; Trapalis, C. *J. Mol. Catal. A: Chem.* **2006**, *249*, 135.
(27) Wang, Z. M.; Yang, G. X.; Biswas, P.; Bresser, W.; Boolchand, P. *Powder Technol.* **2001**, *114*, 197.
(28) Berger, H.; Tang, H.; Lévy, F. *J. Cryst. Growth* **1993**, *130*, 108.
(29) Zhong, J.; Chen, F.; Zhang, J. L. *J. Phys. Chem. C* **2010**, *114*, 933.
(30) Caceres, C. V.; Fierro, J. L. G.; Lazaro, J.; Agudo, A. L.; Soria, J. *J. Catal.* **1990**, *113*, 122.
(31) Sing, K. S. W.; Everett, D. H.; Haul, R. A. W.; Moscou, L.; Pierotti, R. A.; Rouquérol, J.; Siemieniewska, T. *Pure Appl. Chem.* **1985**, *57*, 603.
(32) Wu, T. X.; Liu, G. M.; Zhao, J. C.; Hidaka, H.; Serpone, N. *J. Phys. Chem. B* **1998**, *102*, 5845.
(33) Watanabe, T.; Takizawa, T.; Honda, K. *J. Phys. Chem.* **1977**, *81*, 1845.
(34) Takizawa, T.; Watanabe, T.; Honda, K. *J. Phys. Chem.* **1978**, *82*, 1391.
(35) Zhuang, J. D.; Dai, W. X.; Tian, Q. F.; Li, Zh. H.; Xie, L. Y.; Wang, J. X.; Liu, P. *Langmuir* **2010**, *26*, 9686.
(36) Ren, L.; Ma, L. L.; Jin, L.; Wang, J. B.; Qiu, M. Q.; Yu, Y. *Nanotechnology* **2009**, *20*, 405602.
(37) Peng, X.-T. *Inorganic Chemistry*; Advanced Education Press: Beijing, 1996.
(38) Chen, Ch.; Li, X.; Ma, W.; Zhao, J. C.; Hidaka, H.; Serpone, N. *J. Phys. Chem. B* **2002**, *106*, 318.
(39) Cao, Y. A.; Yang, W. S.; Zhang, W. F.; Liu, G. Z.; Yue, P. *New. J. Chem.* **2004**, *28*, 218.
(40) Cong, Y.; Zhang, J. L.; Chen, F.; Anpo, M.; He, D. N. *J. Phys. Chem. C* **2007**, *111*, 10618.
(41) Xin, B. F.; Jing, L. Q.; Ren, Z. Y.; Wang, B. Q.; Fu, H. G. *J. Phys. Chem. B* **2005**, *109*, 2805.